doi:10.20944/preprints202207.0413.v1

Article

Studies on the Structure and Optical Properties of $BaSrMgWO_6$ Thin Films Deposited by A Spin Coating Method

Luciana Punga[1], Abderrahmane Abbassi[2*], Mihaela Toma[1], Teodor Alupului[1], Corneliu Doroftei[3], Marius Dobromir[4], Daniel Timpu[5], Florica Doroftei[5], Laura Hrostea[6], George G. Rusu[1], Abdelati Razouk[7] and Felicia Iacomi[1*]

[1] Faculty of Physics, Alexandru Ioan Cuza University of Iasi, 11 Carol I Blvd., Iasi 700506, Romania luciana_punga@yahoo.com, toma.mihaela91@yahoo.com, teodor.alupului@yahoo.ro, rusugxg@uaic.ro, iacomi@uaic.ro
[2] LRPSI, Polydisciplinary Faculty of Beni-Mellal, Moulay Slimane University, Mghila BP: 592 Beni Mellal Morocco abbassi.abder@gmail.com
[3] CERNESIM-ICI, Alexandru Ioan Cuza University of Iasi, 11 Carol I Blvd., Iasi 700506, Romania docorneliu@yahoo.com
[4] Department of Research, Faculty of Physics, Alexandru Ioan Cuza University of Iasi, 11 Carol I Blvd., Iasi 700506 Romania marius.dobromir@uaic.ro
[5] Petru Poni Institute of Macromolecular Chemistry, 1A Grigore Ghica Voda Alley 700487 Iasi, Romania dtimpu@icmpp.ro, florica.doroftei@icmpp.ro
[6] RAMTECH, Alexandru Ioan Cuza University of Iasi, 11 Carol I Blvd., 700506, Iasi, Romania laura.hrostea@yahoo.ro
[7] LGEM, FST, Sultan Moulay Slimane University, BP 523, 23000, Beni-Mellal, Morocco razouk.abdelati@gmail.com
*Corresponding author: abbassi.abder@gmail.com; Tel: +212 6 33631269; iacomi@uaic.ro; Tel: +40745076961

Abstract: Highly transparent thin films with the chemical formula $BaSrMgWO_6$ were deposited by spin coating using a solution of nitrates of Ba, Sr and Mg and ammonium paratungstate in dimethylformamide with a ratio Ba:Sr:Mg;W=1:1:1:1. XRD, SEM, EDX and XPS investigations evidenced that an annealing at 800 ºC for 1h leaves the structure amorphous with a precipitate on the surface and that a supplementary annealing at 850 ºC for 45 min forms a nanocrystalline structure and dissolves a part of precipitates. It was evidenced a textured double perovskite cubic structure (61.9%) decorated with tetragonal and cubic impurity phases (12.7 %) like BaO_2, SrO_2 and MgO and an under-stoichiometric phase (24.4%) with the chemical formula $Ba_{2-(x+y)}Sr_xMg_yWO_5$. From transmittance measurements the values of optical band gap were estimated for the amorphous (E_g= 5.15) and nanocrystalline (E_g=4.58 eV) phases. The presence of a lattice disorder was indicated by the high values of Urbach and weak absorption tail energies A decrease in their values was observed and attributed to the crystallization process and cation redistribution.

Keywords: thin films; double perovskite; tungstate; structure; optical properties

1. Introduction

Materials with perovskite structure have been widely studied due to their numerous applications in many technological devices. Perovskites have a stoichiometry of ABX_3, where A cation (alkali or alkali earth metal, large with low charge) is 12 coordinated, the B cation (more electronegative with small radius) is 6 coordinated, and the X anion (oxygen or other anions) is coordinated by two B cations and four A cations [1-5].

Perovskite structure can be altered by substituting multiple cations at either the A- or the B-sites. Ordering of the octahedral site cations and A-site cations in $A_2BB'X_6$ perovskites was analyzed by many authors that showed the alterations of the symmetry of both the undistorted aristotype and the distorted hettotypes and that ordering of A-site cations is typical for anion deficient perovskites [6-9].

Double perovskite structures can be derived from the perovskite structure when half of B site cations are replaced by another B' cation, giving rise to the $A_2BB'X_6$ formula, where A site can be occupied by Ca, Ba, Pb, Sr, Na and B site, that is a 6-fold coordinated transition metal ion or a light alkaline earth ion like Mg, can be also occupied by Ti, Sn, W, Zr, Nb and Ta.[10].

Double perovskite structures are interesting due to their chemical flexibility that offers the possibility to control their properties. Some recent works considered these materials as a new generation of materials which can make a great change and the evolution of material properties [11].

The structure and properties of double perovskite materials with either $A_2BB'O_6$ or $AA'BB'O_6$ stoichiometry are dependent on cations distribution over the octahedral sites, degree of cation inversion as well as on the size and electronic structure of transition metal cations B and B' [12-15].

Some structural studies performed on $BaSrMWO_6$ (M=Ni, Co, Mg) double perovskite oxides showed that the stable crystalline phase is the cubic one with the space group Fm-3m [16]. Other studies performed on $Ba_{2-x}Sr_xCoWO_6$ showed that by increasing the Sr content a phase transition from cubic Fm-3m to tetragonal I4/m, and ultimately monoclinic P21/n takes place, being possible that at room temperature to have a mixture of phases [17]. It was suggested that A^{2+} ions have significant effect in the formation of A_2MgWO_6 structure: a smaller ionic radius of A^{2+} favors a more distorted lattice, and a larger A^{2+} favors cubic phase [18].

The stability and eventual distortion of the structure can be evaluated by using Goldschmidt's tolerance factor, which is useful in evaluating the types of oxides in the perovskite. for an $A_{2-x}A'_xBB'O_6$ double perovskite series using the equation [19, 20]:

$$t = \frac{\left(1 - \frac{x}{2} r_A\right) + \frac{x}{2} r_{A'} + r_O}{\sqrt{2}\left(\frac{x}{2} r_B + \frac{x}{2} r_{B'} + r_O\right)} \tag{1}$$

where r_A, $r_{A'}$, r_B, and $r_{B'}$ are the ionic radii of the A and B sites, and r_O is the ionic radius of oxygen.

Depending on the value of t, the crystal structure may be diverse: for t > 1.05 is hexagonal; for 1.05 > t > 1.00 is cubic (Fm-3m); for 1.00 > t > 0.97 is tetragonal (I4/m) and for t <0.97 is monoclinic (P21/n) or orthorhombic [20].

Until now no study was performed on thin films having the chemical formula $BaSrMWO_6$ (M=Ni, Co, Mg), all the structural studies being performed on ceramics obtained by solid reaction [16-21].

The double perovskites, synthesized by solid-state reaction or coprecipitation methods, with the chemical formula Ba_2MgWO_6, Ba_2BWO_6 (B=Co, Ni, Zn) or other related systems have shown great dielectric properties or high temperature sensitivity [22, 23].

Because these materials may have applications in devices for modern electronics, photovoltaics, and sensors we present in this paper our preliminary results obtained for $BaSrMgWO_6$ thin films deposited by spin coating on quartz and Si p substrates.

In this paper, we will focus our interest to understand the structure and optical properties making a comparison study between previous studies on bulk and actual thin films.

Before the experiment preparation, a theoretical study on $BaSrMgWO_6$ ceramic obtained by solid state reaction, based on the DFT was performed to have an idea on the electronic properties by the extraction of the band structure using WIEN2Kk Code [24].

2. Experimental Section

In a previous study $BaSrMgO_6$ samples were prepared using a solid-state reaction and for the first time the optical properties were investigated [24]. For this study we intended to deposit thin films with chemical formula $BaSrMgO_6$. For thin films deposition we prepared preliminary solutions of nitrates of Ba, Sr and Mg and ammonium paratungstate in dimethylformamide and formed a deposition solution by mixing the preliminary solutions to have a ratio Ba:Sr:Mg;W=1:1:1:1.

For thin film deposition we used a home-made spin coater using a speed of 3000 rot/min for 40 seconds for every layer. Quartz and (111) Si p substrates were used and after every deposition the samples were heated at 100 ºC for 3 min and at 200 ºC for 5 min. The deposition process was 10 times repeated and finally the samples were annealed at 800 ºC for 1h, resulting the sample BSMWO-I. Because the sample BSMWO-I had an amorphous structure the annealing process was repeated at 850 ºC for 45 min the resulted sample being BSMWO-II (Table 1).

The structure of deposited thin films was analyzed by a Shimadzu LabX XRD-6000 Diffractometer with Cu Kα radiation (λ = 1.54059 Å) in Bragg–Brentano configuration. XRD patterns were recorded in the 2θ range of 10–80 degrees with a scan speed of 0.6 deg/min. A Verios G4 UC Scanning Electron Microscope (Thermo Fisher Scientific) equipped with an energy dispersive spectrometer (EDS, EDAX Octane Elite) was used for thin film morphology and elemental chemical composition. For this investigation, a Pt layer was deposited to avoid the electrostatic charge to accumulate on the sample surface.

The information about the surface elemental chemical composition and chemical and electronic states of elements was extracted from the XPS spectra registered with a SPHY-ULVAC VersaProbe 5000 equipment (AlKα, 1486.6 eV). The thin film surfaces were contaminated by free carbon from the air, hence, C 1s peak at 284.6 eV was used as a reference for all binding energies. The high resolution XPS spectra of Ba 3d, Sr 3d, Mg 1s, W 4f and O 1s were fitted with CasaXPS, using a Shirley background subtraction and mixed Gaussian–Lorentzian peak shapes.

The optical properties of thin films were examined in the wavelength range of 200 nm to 1200 nm by a double beam Shimadzu 2450 UV-Vis spectrophotometer, to obtain information about the band gap, Urbach energy, and weak absorption tail energy.

3. Results and Discussion

3.1. Structural investigation

XRD patterns of thin films deposited on quartz are shown in Figure 1. XRD patterns evidence for the BSMWO-I sample an amorphous structure and for the sample BSMWO-II a nanocrystalline structure containing the XRD peaks typical for the face-centered cubic structure of BaSrMgWO6 and some impurity XRD peaks, located at 2θ values of 26.70 º and 27.49 º respectively (noted with * and ** respectively in Figure 1), that generally are attributed to some impurity phases like $MeWO_4$ and Me_2WO_5 (Me=Ba, Sr, Mg). The presence of some BaO_2, SrO_2 and MgO phases that may have a contribution to these XRD peaks may be caused by the formation of some under-stoichiometric phases [25-30].

Crystallographica Search-Match helped us in finding the XRD patterns of tetragonal BaO_2 (F4/mmm, Pdf 3-1130), of tetragonal SrO_2 (P, pdf 3-872) XRD and of cubic MgO (Fm-3m, Pdf 75-1525), close to the XRD pattern of thin film BSMWO-II. Their XRD peaks may have a contribution to the XRD peaks observed at 2θ values of 26.70 º, 27.49 º and 43.25 º respectively.

The XRD pattern of BSMWO-II was identified with the help of Crystallographica Search-Match and XRD peaks belonging to cubic phase Fm-3m were indexed according to PDF 01-080-3482 [16]. For the unit cell parameter of the cubic double perovskite phase, we obtained the value a=b=c=0.81954 nm, that is close to the value obtained previously for the bulk material (a=0.8017 nm) but higher [16, 22].

The crystallite size value was determined for all the XRD peaks observed for double perovskite cubic phase with the Debye–Scherrer equation [31]:

$$D = \frac{0.9 \cdot \mathring{A}}{\beta cos\theta} \tag{2}$$

where D is the particle size, λ is the wavelength (1.5405 Å), β is the full width at half maximum and θ is the Bragg angle. The crystallite sizes varied between 77.4 and 32.43 nm, the medium value, D_m being 44.90 nm (Table 1).

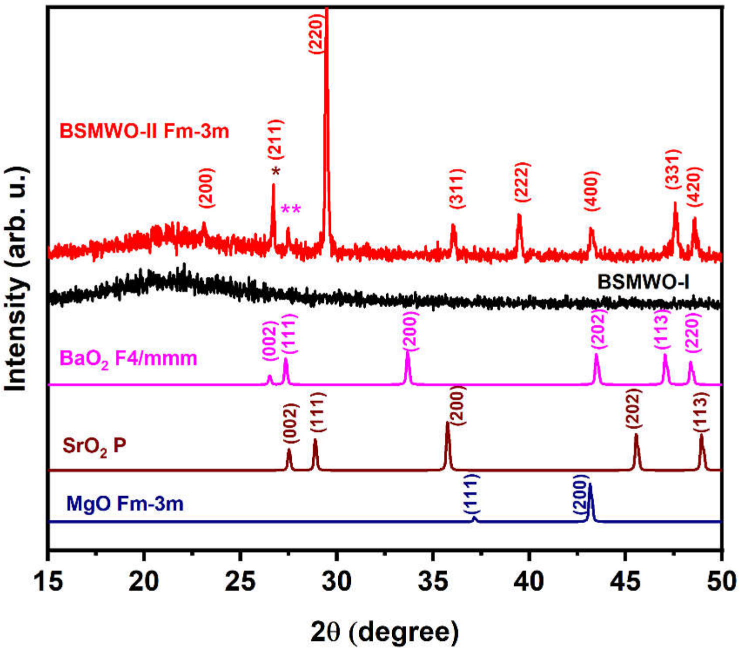

Figure 1. XRD pattern of thin films deposited by spin coating and annealed at different temperatures: BSMWO-I -black line, 800ºC, 1h; BSMWO-II – red line, 800 ºC, 1h and 850 ºC, 45 min. XRD patterns are compared with three possible impurity phases that may exist. The XRD peaks noted with * and ** could have contributions from the tetragonal BaO_2 and SrO_2 phases.

Table 1. Structural characterization of thin films.

Sample	Post deposition annealing	a Å	V $Å^3$	D_m nm	Symmetry	Tolerance factor, t
BSMWO-I	800 ºC, 1h	-	-		amorphous	
BSMWO-II	800 ºC 1h and 850 ºC, 45 min	8.1954 ±0.0757	550.436 ±15.257	44.90 ±0.05	Fm-3m	1.012±0.05

The tolerance factor was calculated using equation (1) with following ionic radii values 1.49 Å, 1.32 Å, 0.86 Å, 0.74 Å, and 1.35 Å for Ba^{2+}, Sr^{2+}, Mg^{2+}, W^{6+}, and O^{2-}, respectively, and was found to be 1.012 for the cubic crystalline sample, when x = 1.

The cubic structure is sustained by the lack of the splitting of the (h00)-type and (hhh)-type reflections.

Comparing the thin film XRD pattern with the XRD patterns previously observed for the bulk $BaSrMgO_6$ structure, obtained by using the solid-state reaction method, we observe a preferential orientation of crystalline planes (220) perpendicular to the substrate and a shift to lower 2θ values [32]. The shift of XRD peaks (220), (311) to lower 2θ values and of XRD peaks (331) and (420) to higher 2θ values may indicate a variation in cation distribution in A type and B type sites in comparison with the cubic structure of $BaSrMgWO_6$ previously obtained by solid state reaction [16].

3.2. Morphology and elemental chemical composition

Figure 2 (a - d) shows SEM images of BSMWO-I and BSMWO-II thin films deposited on quartz (Figure 2 a, b) and on Si p (Figure 2 c, d). It is visible the amorphous character of sample BSMWO-I and the presence of cubic and some tetragonal crystallites formed after the annealing at 850 ºC in sample BSMWO-II.

Before the secondary annealing, BSMO-I films exhibit a slightly granular structure (Figure 2 (a, c)), which can be assigned to their columnar growth on substrates and some

doi:10.20944/preprints202207.0413.v1

spherical particles on the surface. Formation of some precipitates on the thin film surface was also observed in the literature [33].

Some cracks are visible in the SEM image of sample BSMWO-I deposited on glass. They appeared due to the different thermal expansion coefficients of quartz and BSMWO thin film.

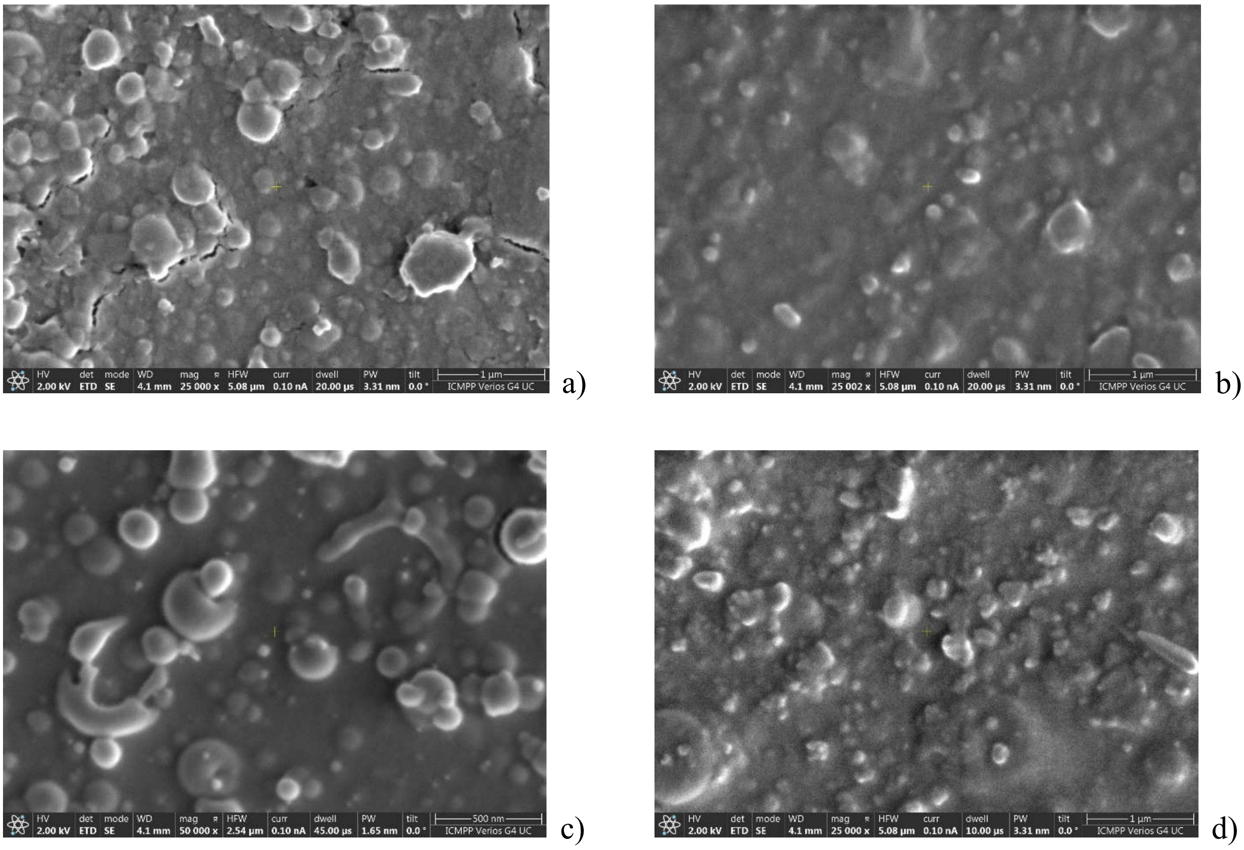

Figure 2. SEM images: (a) BSMWO-I on quartz substrate; (b) BSMWO-II on quartz substrate; (c) BSMWO-I on (111) Si p substrate; (d) BSMWO-II on (111) Si p substrate.

No cracks were observed on the surface of BSMWO-I thin film deposited on (111) Si p indicating smaller tensions in comparison to quartz substrate.

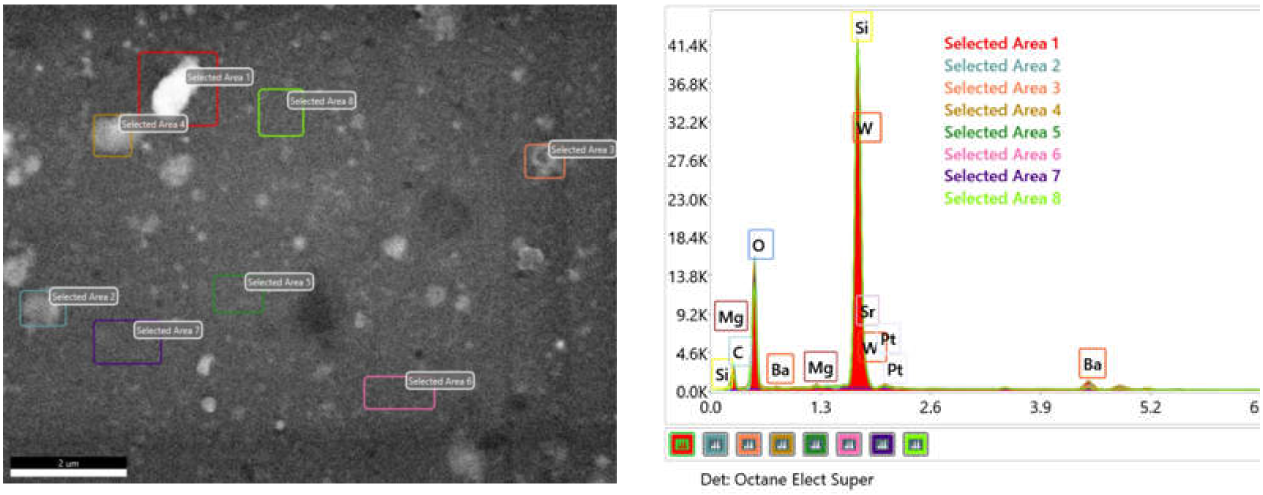

a)

b)

Figure 3. EDX spectra belonging to 8 different area of BSMWO-II SEM image:(a) SEM image; (b) EDX spectra. The investigated area and the coresponding spectra are marked with the same collors.

SEM images of thin films BSMWO-II deposited on quartz and (111) Si p (Figure 2 b, d), that have a supplementary annealing at 850 ºC for 45 min, show that most of the globular precipitates become tetragonal or cubic and smaller in size and exhibit a preferential orientation in the thin film plane (parallel to [220] axis) in agreement with XRD pattern. This fact suggests that a part of precipitates was dissolved into the lattice and that the tensions between the substrate and thin film become smaller (no cracks were observed for quartz substrate).

Table 2. EDX chemical elemental composition of thin film BSMWO-II.

Elements	**Area 1 Atomic %**	**Area 2 Atomic %**	**Area 3 Atomic %**	**Area 4 Atomic %**	**Area 5 Atomic %**	**Area 6 Atomic %**	**Area 7 Atomic %**	**Area 8 Atomic %**
C K	34.6	31.1	30.4	34.1	28.5	27.8	28.7	30
O K	44.1	46.6	47	44.7	47.6	47.3	47.5	46.3
Si K	19.6	20.9	21.2	19.3	22.7	22.8	22.6	22.5
Mg K	0.2	0.3	0 .3	0.3	0.3	0.3	0.3	0.3
Sr L	0.3	0.3	0.3	0.3	0.2	0.4	0.4	0.4
Ba L	0.8	0.5	0.4	0.8	0.2	0.2	0.2	0.2
W L	0.2	0.1	0.2	0.2	0.2	0.2	0.2	0.2
Pt L	0.2	0.2	0.2	0.2	0.2	0.1	0.2	0.2

Figure 3 (a, b) shows the EDX spectra belonging to different area of BSMWO-II, that confirm that the sample contains all elements of the raw material inputs in comparable contents. In Table 2 are presented the atomic elemental compositions for the investigated area.

By extracting the quartz substrate chemical composition and the surface adventitious carbon it was possible to determine a chemical formula for the thin film and for the surface precipitates. EDX analysis evidenced a possible stoichiometric formula for the double perovskite $BaSrMgWO_6$ and some possible stoichiometric formula for surface oxides like BaO_2, SrO_2 and MgO [33, 34].

These oxides indicate the presence of other possible phases that may result during the deposition and annealing processes and that are also suggested by XRD pattern. Because SEM analysis sustains the ratio W:Ba:Sr:Mg=1:1:1:1 we suppose that a certain percent of oxide phases are the result of the migration of some cations outside the stoichiometric lattice, living an under-stoichiometric lattice according to these two possible chemical relations:

$$BaSrMgWO_6 \rightarrow Ba_{2-(x+y)} Sr_xMg_yWO_5+Ba_{x+y}O+ Sr_{2-x}O +Mg_{2-y}O \quad (3)$$

where $0 \leq x, \leq 2$,

$$BaSrMgWO_6 \rightarrow Ba_{1-(x+y)} Sr_xMg_y WO_5+Ba_{x+y}O+ Sr_{1-x} +Mg_{1-y}O \quad (4)$$

where $0\leq x, y \leq 1$.

The formation of peroxide phases in the conditions we used for thin film deposition and annealing is also possible. since BaO and SrO can easily adsorb oxygen from the air to form BaO_2 and SrO_2.

3.3. Chemical states

XPS surface analysis was focused on determining whether Ba, Sr, and Mg can be found in the stoichiometric or under-stoichiometric double perovskite lattice and in the surface oxides since the registered binding energy of each given element's electron orbital gives the information about its specific chemical state.

Even EDX spectra showed a content of W similar to Ba, Sr amd Mg the high-resolution XPS spectrum of W4f (Figure 4 a) has a small intensity. This situation is caused by the surface species also evidenced by SEM images. The asymmetric broad peak, located at a binding energy higher than that observed for W^{4+} species indicates inhomogeneities in the chemical composition. The presence of superficial oxides indicates the possible existence of W^{5+}. This state can result because of cation migration and the formation of an under-stoichiometric lattice. It was possible to deconvolute the XPS W4f spectrum into two doublets with equal FWHM (2.5 eV) with a $4f_{7/2}$ – $4f5_{/2}$ doublet separation of 2.2 eV and with area ratios of 4:3. The peak positions located at 37.60 eV and 39.73 eV respectively, attributed to $4f_{5/2}$ and $4f_{7/2}$, indicate the W^{6+} state, typical for the W-O bond in the cubic double perovskite structure [35 -38]. The doublet with the XPS peaks located at 36.53 eV and 38.73 eV may be attributed to W^{5+} state. The XPS peak area of W^{5+} represents 38.1 % from the total spectrum.

We performed a deconvolution of XPS spectra in agreement with relation (3) also considering as oxides BaO_2, SrO_2 and MgO, and the result of deconvolution of XPS W 4f spectrum and EDX results.

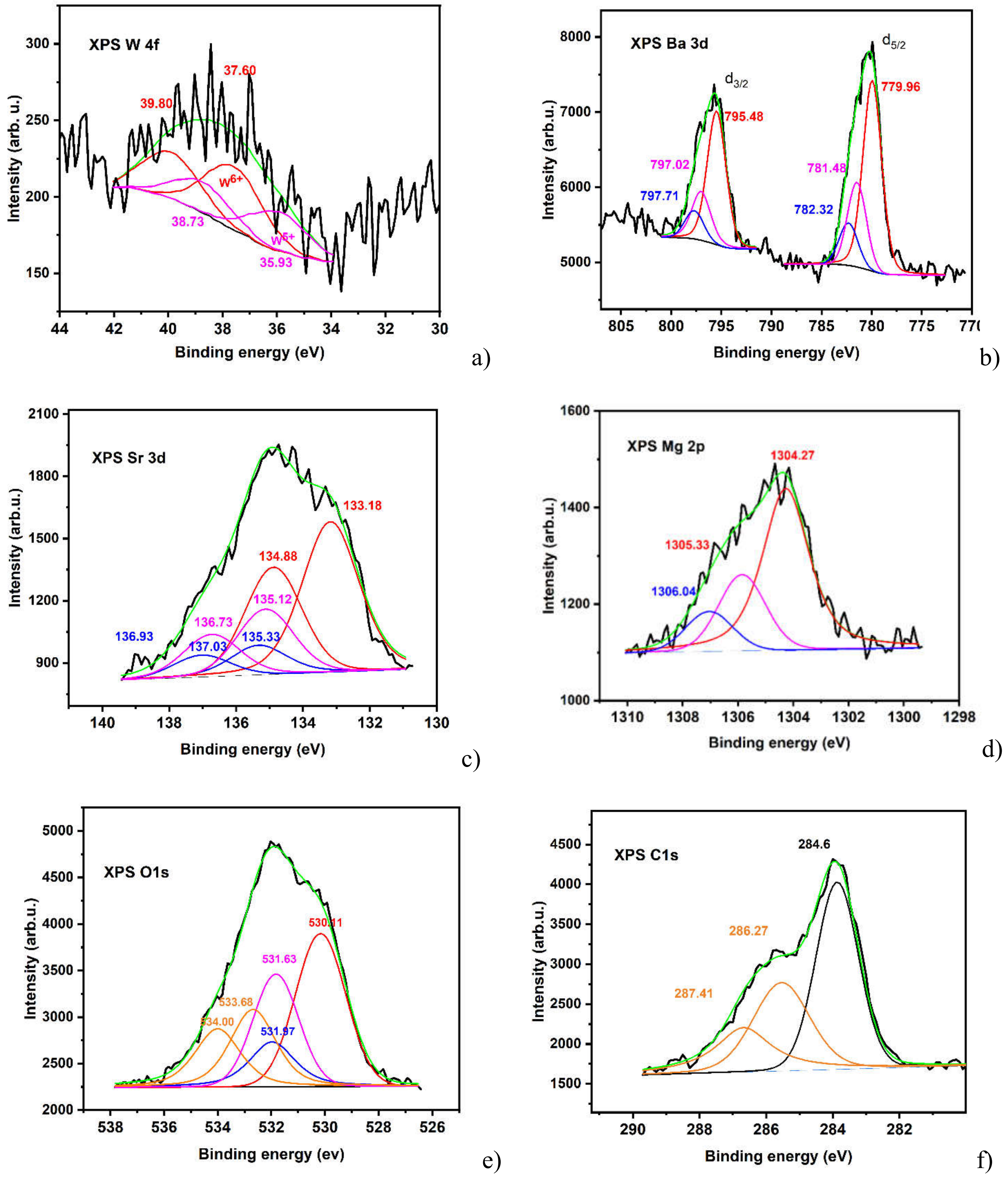

Figure 4. High-resolution XPS spectra of BSMWO-II thin film: (a) Ba 3d; (b) Sr 3d; (c) Mg 1s; (d) W4f; (e) O1s; (f) C 1s. Red line indicates species in cubic coordination in double perovskite structure, blue line indicates surface species, pink line indicates the under-stoichiometric structure and orange line indicates adsorbed species.

The deconvolution of the high-resolution core level Ba 3d, Sr 3d and W 4f spectra was performed also considering the states in an under-stoichiometric structure. For an appropriate fit of Ba 3d, Sr 3d and Mg 1s spectra we included three different species in the fitting routine. We considered the high and low binding energy species as surface and bulk species, respectively. The spin–orbit splitting energy of Ba-3d state was approximately 15.54

eV for all the three species we introduced in the fitting routine, with a $d_{5/2}$ to $d_{3/2}$ intensity ratio of 3: 2. The doublets attributed to different species are separated by approximately 1.8 eV (Fig. 4. a) and 2.25 eV and have the same full width half maximum (FWHM) of 2.2 eV.

Since barium is a highly electropositive element, in barium oxide compounds the state is always 2+ and the chemical shift is a result of local potential change caused by different anion coordination. As the coordination of negative ions is higher the local electron potential increases and the binding energy decreases [39]. In the stoichiometric perovskite structure Ba is 12-fold and, in the under-stoichiometric structure and in peroxide structure is 10-fold, so the binding energy of Ba^{2+} in cubic double perovskite structure will be lower than Ba^{2+} in under-stoichiometric $Ba_{2-(x+y)}$ Sr_xMg_y WO_5 structure or in tetragonal BaO_2 [26, 33, 40]. The attribution of the peaks with higher binding energy to BaO_2 agrees with the results obtained by other authors [33].

The best fit in the deconvolution of XPS Ba 3d was obtained for 61.9 % for Ba^{2+} species in $BaSrMgWO_6$, 25.4% for Ba^{2+} in under-stoichiometric phases of type $Ba_{2-(x+y)}$ $Sr_xMg_yWO_5$ and 12.7 % for surfaces oxides, as we expected (Table 3) [41-43].

Table 3. Binding energies of elements Ba 3d, Sr 3d, Mg 1s, O 1s, C1s observed in BSMWO-II high-resolution spectra, (eV), peak area (%) and attribution.

Compound	BE (eV)								
	Ba 3d		**Sr 3d**		**Mg 1s**	**W 4f**		**O 1s**	**C1s**
	$3d_{5/2}$	**$3d_{3/2}$**	**$3d_{5/2}$**	**$3d3_{/2}$**	**1s**	**$4f_{7/2}$**	**$4f_{5/2}$**	**1s**	**1s**
$BaSrMgWO_6$	779.96	795.48	133.18	134.88	1304.27	37.60	39.90	530.11	
Peak area %	61.9		61.9		61.9	61.9		33.3	
$Ba_{2-(x+y)}$ $Sr_xMg_yWO_5$	781.48	797.02	135.12	136.73	1305.33	35.93	38.73	531.63	
Peak area, %	25.4		25.4		25.4	38.1		22.7	
BaO_2, SrO_2 MgO	782.32	797.71	136.33	137.33	1306.33			531.87	
Peak area, %	12.7		12.7		12.7			11.4	
C-C									284.6
Peak area, %									46.7
OH; C-OH								532.68	286.27
Peak area, %								18.4	31.6
H_2O, O_2 C=O								534.00	287.41
Peak area, %								14.2	21.7

The Sr 3d XPS high resolution spectrum was fitted with three doublets, restricted by an equal FWHM of 2 eV; a fixed doublet separation of 1.7 eV (spin orbit splitting) and an area ratio of $d_{5/2}$ to $d_{3/2}$ of 3:2 [25, 43]. Based on the best fit, the following attributions for the resulted XPS $3d_{5/2}$ peaks were made: 133.14 eV is typical for Sr^{2+} species located in the cubic double perovskite; 135.12 eV is characteristic to Sr^{2+}in a $Ba_{2-(x+y)}$ Sr_xMg_y WO_5 under-stoichiometric lattice, and 135.33 eV is characteristic to Sr^{2+} in the tetragonal lattice of SrO_2 (Figure 4 b, Table 3) [45, 46]. The two peaks belonging to different species are separated by 2.0-2.2 eV. The repartition of different Sr^{2+} species as resulted from the best fit was the same as the repartition of Ba^{2+} species.

Like barium and strontium, magnesium is a highly electropositive element and in oxide compounds its state is Mg^{2+}. For the deconvolution of high-resolution XPS Mg 1s spectrum we used the same repartition of $Mg^{2=}$ species as we already used for Ba^{2+} and Sr^{2+}. The best fit is shown in Figure 4 (d) and the deconvolution results are indicated in Table 3. The obtained results are in good agreement with the literature [33, 34, 46, 47,]. The species were fitted with peaks of equal FWHM (2.2 eV), and an energy separation between peaks of 1.6 eV and 2.8 eV.

For the XPS O1s spectrum was necessary to introduce in the fitting routine five peaks with different FWHM (Figure 4 e, Table 3) The peak with the lowest binding energy of

530.11 eV (2.2 eV) is characteristic for the stoichiometric double perovskite lattice and the peak with the binding energy of 531.87 eV (2.0 eV) is characteristic for surface oxide species. The peak with the binding energy of 531.63 eV is typical for an under-stoichiometric lattice. The other two peaks located at 532.7eV (1.89 eV) and 533.7 eV (2.39 eV) are characteristic for species adsorbed on the surface, like free OH groups and OH in free water molecules and oxygen molecules, O_2. These peaks can be also related to XPS peaks located at 286.27 eV and at 287.42 eV in the high-resolution C 1s spectrum [48, 49].

However, on perovskites surfaces, adsorbed oxygen species may as well play a role [48, 50]. We consider that surface SrO_2 and BaO_2 species cause a separated oxygen surface species in conjunction with hydroxylation.

Table 4. Elemental chemical composition of BSMWO-II thin film.

Compound	Elements, atomic %				
	O	Ba	Sr	Mg	W
BaS rMgWO$_6$	40.39	5.38	5.38	5.38	5.38
$Ba_{2-(x+y)}$ $Sr_xMg_yWO_5$	16.57	2.21	2.21	2.21	3.31
BaO_2, SrO_2, MgO	8.29	1.10	1.1	1.10	0.00
Total	65.25	8.69	8.69	8.69	8.69

The area of XPS peaks, I_j attributed to different elements present in the three species identified as $BaSrMgWO_6$, $Ba_{2-(x+y)}$ $Sr_xMg_yWO_5$ and surfaces oxides (the adsorbed phases and adventitious carbon were neglected) were used to determine the thin film chemical elemental composition in at% using the sensitivity factors S_j (O 1s = 0.733, Sr 3d = 1.992, Ba 3d = 7.343, W 4f = 3.863, Mg 1s = 1.035) and the relation:

$$X_p(\%at) = \frac{I_p/S_p}{\sum_j \frac{I_j}{S_j}} \tag{5}$$

where Xp is the atomic concentration in percent of a certain element.

By correlating XRD, SEM, EDX and XPS results was possible to identify the phases formed in the thin film and have an information about the processes that take place during the annealing.

It is possible to conclude that the result of our experiments is a thin film with a cubic stoichiometric double perovskite structure, with the chemical formula BaStrMgWO$_6$, decorated with an under- stoichiometric layer with the chemical formula $Ba_{2-(x+y)}$ $Sr_xMg_yWO_5$ $0 \le x, y \le 1$ (representing 25.4% from the total chemical composition), and with BaO_2, SrO_2, MgO nanoparticles (representing 12.7%). This thin film may have interesting properties as gas sensor, catalyzer, or as active layer in transparent devices.

3.4. Optical properties

At the interaction of a material with photons a fundamental absorption may appear due to excitonic processes or band-to-band transition [49, 51]. The band-to-band transition at the fundamental edge may be direct or indirect. Previous theoretical and experimental studies performed on bulk $BaSrMgWO_6$ evidenced a direct band-to-band transition and an optical bang gap energy, E_g, of 3.7 eV.

In Figure 5 (a-d) are shown the results obtained from transmittance measurements.

The thin film transmittance is higher than 80% in the UV range and exceeds 90% in the visible range (Figure 5 a). The thin film annealing process at 850 ºC determined the crystallization process and consequently the increase in the absorption coefficient in UV and a red shift of the transmittance spectrum. For BSMWO-II thin film two absorption bands becomes visible at around 350 nm and 450 nm that can be attributed to the charge transfer W^{6+}-O^{2-} and to some distorted $(WO_6)^{6-}$ octahedrons [36].

The absorption coefficient was determined by using the relation generally used for transparent thin films:

$$\alpha = \frac{1}{d} ln\left(\frac{100}{T}\right) \tag{6}$$

where d is the thin film thickness in cm, and T is the transmittance in % [52, 53].

Plots of absorption coefficient versus wavelength are shown in Figure 5 (b). The absorption coefficients increase sharply with decrease in wavelength values. The wavelength dependence of the absorption coefficient of sample BSMWO-II shows higher values compared with absorption coefficient of sample BSMWO-I until 650 nm when its values become comparable and even smaller at higher wavelength values (3177.4 $cm^{-1}$for BSMWO-II and 4409.5 cm^{-1} for BSMWO-I at 800 nm).

For the optical band gap energy determination, we used the Tauc formula for the direct transition [53]:

$$h\nu\alpha = A\left(h\nu - E_g\right)^{1/2} \tag{7}$$

where A is an energy dependent constant, E_g is the optical band gap energy, h is Planck constant, ν is the photon frequency and α is the absorption coefficient.

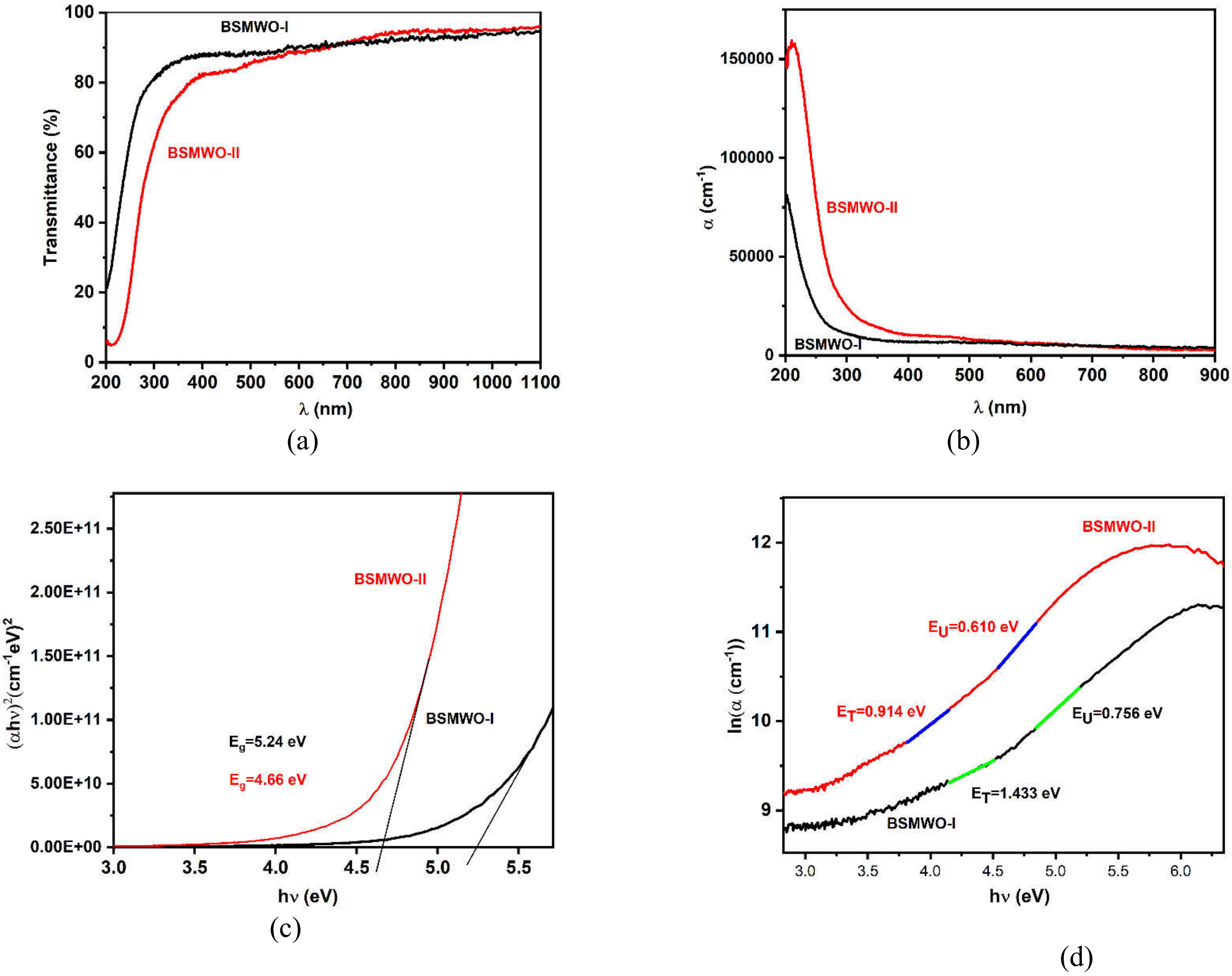

(a)

(b)

(c)

(d)

Figure 5. Optical properties of BSMWO-I and BSMWO-II thin films: (a) transmittance spectra; (b) absorption coefficient; (c) determination of optical band gap energy; (d) determination of Urbach and weak absorption tail energies.

Figure 5 (c) shows the plots of $(h\nu\alpha)^2$ versus hν.

The band gap energies were obtained by fitting a linear line E_g value being determined from the intercept with the photon energy axis. Due to structural changes after the second post deposition annealing (850 ºC, 45 min) the optical band gap energy decreases from $E_g = 5.24$ eV to E_g=4.66 eV. This change in the band gap energy can be attributed not only to the crystallization process but also to some changes in the chemical composition because of cation redistribution.

The values obtained for the band gap energies are higher compared with the value obtained for the bulk ($E_g = 3.7$ eV), possible due to the differences in crystallite sizes and stoichiometry.

During band-to-band transitions due to disorder, density of states in valence and conduction band tails into the energy gap and consequently the absorption coefficient α(E) also tails off in an exponential manner. The energy associated with this tail is referred as Urbach energy and can be calculated by the following equation [54]:

$$\alpha(h\nu) = exp\left(\frac{h\nu}{E_U}\right) \tag{8}$$

There is also a weak absorption tail for those transitions taking place from one localized tail state above the valence band to another localized tail state below the conduction band, in the weak absorption region. The energy associated with this tail is referred as E_T and can be calculated with a relation like equation (6).

Figure 5 (d) shows the plots lnα =f(hν) that allow the determination of E_U and E_T by fitting the linear portion of the curve with a straight line in the Urbach and weak absorption tail regions; the reciprocal of the slopes yielding the values of Eu and E_T, respectively.

Table 5. Thin film optical properties: transmittance, T, absorption coefficient, α, bang gap energy, E_g, Urbach energy, E_U and weak absorption tail energy, E_T.

Sample	d, nm	T (450 nm) %	α (450 nm) cm^{-1}	E_g eV	E_U eV	E_T eV
BSMWO-I	150	88.3	6734.6	5.24	0.756	1.433
BSMWO-II	150	83.3	9705.7	4.66	0.610	0.914

The high values of Urbach energy and weak absorption tail energy indicate disorder in agreement with SEM, EDX and XPS results. The decrease in Urbach and weak absorption tailing with thin film annealing at higher temperature is due to the improvement in crystallinity of the films and elimination of a part of intracrystalline tensions.

5. Conclusion

We succeed to grow by a spin coating method highly transparent thin films with a cubic Fm-3m double perovskite structure with chemical formula $BaSrMgWO_6$.

XRD, SEM, EDX and XPS investigations evidenced that an annealing at 800 ºC for 1h leaves the structure amorphous with a precipitate on the surface. The supplementary annealing at 850 ºC for 45 min succeeds to start the crystallization process and to dissolve a part of precipitates. It was possible to evidence a textured cubic structure (61.9%) and the presence of some tetragonal and cubic impurity phases (12.7%) like BaO_2, SrO_2 and MgO and an under-stoichiometric phase (24.4 %) with the chemical formula $Ba_{2-(x+y)}Sr_xMg_yWO_5$.

Investigation of optical properties enabled to determine the optical band gap and have information about Urbach and weak absorption tail energies. The values obtained for the amorphous (5.24 eV) and nanocrystalline thin films (4.66 eV) are higher compared with the value of 3.7 eV observed in the previous studies for the bulk, possible due to differences in crystallite sizes and defects content.

Considering the interesting properties that the surface peroxide and oxide nanoparticles and under-stoichiometric phase may impose to the thin film, future investigations on sensor, photocatalytic and dielectric properties will be performed. Also, will be interesting to study of the effect of an annealing performed at a higher temperature on the structure and thin film optical properties.

References

[1] Galasso, F.S. *Structure, Properties and Preparation of Perovskite-Type Compounds*. Pergamon Press, Oxford, 1969.

[2] Howard, C.J.; Stookes, H. T. Structures and phase transitions in perovskites - a group-theoretical approach, *Acta Crystallogr. A: Found. Crystallogr*. **2005**, 61, 93–111. https://doi.org/10.1107/S0108767304024493 .

[3] Howard, C. J.; Kennedy, B. J.; Woodward, P. M. Ordered double perovskites - a group-theoretical analysis, *Acta Crystallogr B* **2003,** 59 (Pt 4), 463-71. https://doi.org/10.1107/s0108768103010073.

[4] Doroftei, C.; Popa, P. D.; Iacomi, F.; Leontie, L.; The influence of Zn^{2+} ions on the microstructure, electrical and gas sensing properties of $La_{0.8}Pb_{0.2}FeO_3$ perovskite. *Sens. Actuators B Chem.* **2014**, 191, 239-245. https://doi.org/10.1016/j.snb.2013.09.113.

[5] Rezlescu, N.; Rezlescu, E.; Popa, P. D.; Doroftei, C.; Ignat, M.; Partial substitution of manganese with cerium in $SrMnO_3$ nano-perovskite catalyst. Effect of the modification on the catalytic combustion of dilute acetone. *Mater. Chem. Phys.* **2016**, 182, 332-337. http://dx.doi.org/10.1016/j.matchemphys.2016.07.040.

[6] Knapp, M. C. P.; Woodward, M. A-site cation ordering in AA'BB'O_6 perovskites, *J. Solid State* ***Chem.*** **2006,** 179, 1076–1085. https://doi.org/10.1016/j.jssc.2006.01.005**.**

[7] Davies, P.K. Cation ordering in complex oxides, *Curr. Opin. Solid State Mater. Sci*. **1999**, 4, 467–471.

[8] Karen, P.; Kjekshus, A.; Huang, Q.; Lynn, V. L. W.; Rosov, N.; Natali Sora, I.; Santoro, A. Neutron powder diffraction study of nuclear and magnetic structures of oxidized and reduced $YBa_2Fe_3O_{8+w}$, *J. Solid State Chem.* **2003**, 174 (1), 87-95, https://doi.org/10.1016/S0022-4596(03)00180-4.

[9] Barnes, P.W.; Lufaso, M.W.; Woodward, P.M. *Acta Crystallogr B* Structure prediction of ordered and disordered multiple octahedral cation perovskites using SPuDS. **2006**, 62, 397-410. https://doi.org/10.1107/S010876810600262X.

[10] Saha-Dasgupta, T.; Double perovskites with 3d and 4d/5d transition metals: compounds with promises. *Mater. Res. Express* **2020**, 7, 014003.

[11] Hossain, A.; Bandyopadhyay, P.; Roy, S. An overview of double perovskites $A_2B'B''O_6$ with small ions at A site: Synthesis, structure and magnetic properties. *J. Alloys Compd.* **2018**, 740, 414-427. https://doi.org/10.1016/j.jallcom.2017.12.282.

[12] Manoun, B.; Ezzahi, A.; Benmokhtar, S.; Ider, A.; Lazor, P.; Bih, L.; Igartua, J.M.; Gemmill, W.R.; Smith, M.D.; Zur Loye, H.-C. X-ray diffraction and Raman spectroscopy studies of temperature and composition induced phase transitions in $Ba_{2-x}Sr_xZnWO_6$ ($0 \leq x \leq 2$) double perovskite oxides, *J. Solid State Chem.* **2004**, 177, 3560. https://doi.org/10.1016/j.jallcom.2012.03.075.

[13] Bugaris, D. E.; Hodges, J. P.; Huq, A.; Loye, H.-C. Crystal growth, structures, and optical properties of the cubic double perovskites Ba_2MgWO_6 and Ba_2ZnWO_6, *J. Solid State Chem.* **2011**, 184, 2293-2298. https://doi.org/10.1016/j.jssc.2011.06.015.

[14] Khalyavin, D.D.; Han, J.; Senos, A. M. R.; Mantas, P.Q. Synthesis and dielectric properties of tungsten-based complex perovskites, *J. Mater. Res.* **2003**, 18, 2600-2607. https://doi.org/10.1557/JMR.2003.0364.

[15] Fu, W.T.; Akerboom, S.; IJdo, D.J.W. Crystal structures of the double perovskites $Ba_2Sr_{1-x}Ca_xWO_6$, *J. Solid State Chem*. **2007**, 180, 1547–1552. https://doi.org/10.1016/j.jssc.2007.03.008.

[16] Ezzahi, A.; Manoun, B.; Ider, A.; Bih, L.; Benmokhtar, S.; Azrour, M.; Azdou, M.; Igartua, J.M. Lazor, P. X-ray diffraction and Raman spectroscopy studies of $BaSrMWO_6$ (M=Ni, Co, Mg) double perovskite oxides, *J. Mol. Struct.* **2011**, 985, 339–345. https://doi.org/10.1016/j.molstruc.2010.11.017.

[17] Zhou, Q.; Kennedy, B. J.; Elcombe, M. M. Composition and temperature dependent phase transitions in Co–W double perovskites, a synchrotron X-ray and neutron powder diffraction study, *J. Solid State Chem.* **2007**, 180, 541–548.

[18] Khattak, C.P.; Hurst, J.J.; Cox, D.E. Crystal growth, and electrical and magnetic properties of Ba_2CoWO_6, *Mater. Res. Bull.* **1975**, 10 (12), 1343-1347. https://doi.org/10.1016/0025-5408(75)90095-1.

[19] Depianti, J.B; Orlando, M.; Cavichini, A.; Correa, H.P.S.; Rodrigues, V.A.; Passamai, J. L.; Piedade, E. L. O.; Belich, H.; Medeiros, E.F.; De Melo, F.C.L; Structural and magnetic investigation of Ca_2MnReO_6 doped with Ce. *Ceramica* **2013**, 59, 262–268. https://doi.org/10.1590/S0366-69132013000200011.

[20] Alsabah, Y. A.; AlSalhi, M. S.; Mustafa, E. M.; Elbadawi, A. A.; Devanesan, S.; Siddig, M. A.; Synthesis, Phase Transition, and Optical Studies of $Ba_{2-x}Sr_xZnWO_6$ (x = 1.00, 1.25, 1.50, 1.75, 2.00) Tungsten Double Perovskite Oxides, *Crystals* **2020**, 10, 299. https://doi.org/10.3390/cryst10040299.

[21] Patwe, S.J., Achary, S.N.; Mathews, M.D.; Tyag A.K., Synthesis, phase transition and thermal expansion studies on M_2MgWO_6 (M = Ba $^{2+}$ and Sr $^{2+}$) double perovskites, *J. Alloys Compd*. **2005**, 390, 100–105. https://doi.org/10.1016/j.jallcom.2004.05.093.

[22] Chen, Y.C.; Wang, Y.N.; Syu, R.Y. Effect of sintering temperature on microstructures and microwave dielectric properties of Ba_2MgWO_6 ceramics. *J. Mater. Sci. Mater. Electron*. **2016**, 27, 4259–4264.

[23] Vu, Q. T. H.; Bondzior, B.; Stefanska, D.; Miniajluk-Gaweł, N.; Winiarski, M. J.; Deren, P. J. On how the mechanochemical and co-precipitation synthesis method changes the sensitivity and operating range of the $Ba_2Mg_{1-x}Eu_xWO_6$ optical thermometer, *Sci. Rep*. 2021, 11, 22847. https://doi.org/10.1038/s41598-021-02309-9.

[24] Abbassi, A. Opto-electronic Properties of the co-doped ZnO, Perovskites $BiMO_3$ and New Cubic Double Perovskite $BaSrMgWO_6$ Oxides: Theory and Experiment. PhD thesis, Universite Mohammed V, Faculte des Sciences, Rabat, 2016.

[25] Opitz, A. K.; Rameshan, C.; Kubicek, M.; Rupp, G. M.; Nenning, A.; Götsch, T.; Blume, R.; Hävecker, M.; Knop-Gericke,·A.; Rupprechter, G.; Klötzer, B.; Fleig, J. The Chemical Evolution of the $La_{0.6}Sr_{0.4}CoO_{3-\delta}$ Surface Under SOFC Operating Conditions and Its Implications for Electrochemical Oxygen Exchange Activity. *Top. Catal.* **2018**, 61, 2129–2141. https://doi.org/10.1007/s11244-018-1068-1.

[26] Zhu, Y.; Liu, D.; Jing, H.; Zhang, F.; Zhang, X.; Hu, S.; Zhang, L.; Wang, J.; Zhang, L.; Zhang, W.; Pang, B.; Zhang, P.; Fan, F.; Xiao, J.; Liu, W.; Zhu, X.; Yang, W. Oxygen activation on Ba-containing perovskite materials, *Sci. Adv*. **2022**, 8, eabn4072, 1-9.

[27] Wu, J. Y.; Bian, J. J. Structure stability and microwave dielectric properties of double perovskite ceramics – $Ba_2Mg_{1x}Ca_xWO_6$ ($0.0 \leq x \leq 0.15$), *Ceram. Int.* **2012**, 38, 3217–3225. https://doi.org/10.1016/j.ceramint.2011.12.027.

[28] Natl. Bur. Stand. (U.S.) Monogr. **1982**, 25 (19), 21.

[29] Natl. Bur. Stand. (U.S.) **1956**, 539 (6), 52.

[30] Hanawalt, J. D.; Rinn, H.W.; Frevel, L.K. Chemical Analysis by X-Ray Diffraction, *Anal. Chem*. **1938**, 10, 475-512.

[31] Yildiz, A.; Irimia, M.; Toma, M.; Spulber, I.; Zodieriu, G.; Dobromir, M.; Timpu, D.; Iacomi, F. Effect of the Substrate Nature on Electron Transport in Ga Doped ZnO Thin Films Grown by RF Sputtering, *Mater. Today Proc*. **2018**, 5, 15888–15894.

[32] Kumar, S.; Sharma, S. K.; Alimuddin, Knobel, M.; Choudhary, R.J.; Lee, C. G.; Koo, B.H.; Kumar, R. Structural and magnetic properties of bulk and thin films of $Mg_{0.95}Mn_{0.05}Fe_2O_4$. *Curr. Appl. Phys.* **2009**, 9, 1009–1013. https://doi.org/10.1016/j.cap.2008.11.001.

[33] Droubay, T.C.; Kong, L.; Chambers, S.A.; Hes, W.P.; Work function reduction by BaO: Growth of crystalline barium oxide on Ag(001) and Ag(111) surfaces. *Surf. Sci*. **2015**, 632, 201-206.

[34] Wong-Ng, W.; Roth, R. S. Single-crystal structural investigation of BaO_2. *Phys. C: Supercond. Appl*. **1994**, 233 (1–20), 97-101. https://doi.org/10.1016/0921-4534(94)00562-1.

[35] De Angelis, B. A.; Schiavello, M. X-ray photoelectron spectroscopy study of nonstoichiometric tungsten oxides. *J. Solid State Chem.* **1977**, 21, 67-72.

[36] Wang, S.; Gao, H.; Chen, C.; Li, Q.; Li, C.; Wei, Y.; Fang, L. Effect of phase transition on optical and photoluminescence properties of nano-$MgWO_4$ phosphor prepared by a gamma-ray irradiation assisted polyacrylamide gel method. *J. Mater. Sci: Mater. Electron*. **2019**, 30, 15744–15753. https://doi.org/10.1007/s10854-019-01960-3.

[37] Vasilopoulou, M.; Soultati, A.; Georgiadou, D. G.; Stergiopoulos, T.; Palilis, L. C.; Kennou, S.; Stathopoulos, N. A.; Davazoglou, D.; Argitis, P. Hydrogenated under-stoichiometric tungsten oxide anode interlayers for efficient and stable organic photovoltaics. J. *Mater. Chem*. A 2 (2014) 1738-1749.

[38] de Angelis, B. A.; Schiavello, M. X-Ray Photoelectron Spectroscopy Study of Nonstoichiometric Tungsten Oxides, *J. Solid State Chem.* **1977**, 21, 67-72.

[39] Hung, C. C.; Riman, R. E. An XPS Investigation of Hydrothermal and Commercial Barium Titanate Powders, *KONA Powder Part. J.* **1990**, 8, 99-104.

[40] Jha, D.; Himanshu, A. K.; Singh, B. K.; Shukla, D.; Kuma, U.; Kumar, R.; Bhattacharyya, K.; Shinde, A. B.; Krishna, P. S. R.; Dutta, A.; Sinha, T. P.; Ray, R. The X-ray photoelectron and Co K -Edge absorption spectra of Ba_2CoWO_6. https://arxiv.org/ftp/arxiv/papers/1907/1907.00342.pdf.

[41] Wlodarczyk, D.; Amilusik, M.; Kosyl, K. M.; Chrunik, M.; Lawniczak-Jablonska, K.; Strankowski, M.; Zajac, M.; Tsiumra, V.; Grochot, A.; Reszka, A.; Suchocki, A.; Giela, T.; Iwanowski, P.; Bockowski, M.; Przybylinska, H.; Synthesis Attempt and Structural Studies of Novel A_2CeWO_6 Double Perovskites (A^{2+} = Ba, Ca) in and outside of Ambient Conditions. *ACS Omega* **2022**, 27, 18382−18408.

[42] Cai, Z.; Kubicek, M.; Fleig, J.; Yildiz, B. Chemical heterogeneities on $La_{0.6}Sr_{0.4}CoO_{3-\delta}$ thin films—correlations to cathode surface activity and stability. *Chem Mater* **2012**, 24(6), 1116–1127. https://doi.org/10.1021/cm203501u.

[43] Jantz, S. G.; Pielnhofer, F.; Dialer, M.; Höppe, H. A. On Tungstates of Divalent Cations (I) – Structural Investigation and Spectroscopic Properties of $Sr_2[WO_5]$ and $Ba_2[WO_5]$. *Z. Anorg. Allg. Chem.* **2017**, 643, 2024–2030. http://dx.doi.org/10.1002/zaac.201700334.

[44] Triyono, D.; Hannisa, A.; Laysandra, H. Structural, magnetic, and dielectric studies of cubically ordered Sr_2FeMnO_6. *Appl. Phys. A* **2022**, 128, 232 1-8. https://doi.org/10.1007/s00339-022-05372-9.

[45] Kim, D.; Bliem, R.; Hess, F.; Gallet, J.-J.; Yildiz, B. Electrochemical polarization dependence of the elastic and electrostatic driving forces to aliovalent dopant segregation on $LaMnO_3$, *J. Am. Chem. Soc.* **2020**, 142 (7), 3548–3563. http://dx.doi.org/10.1021/jacs.9b13040.

[46] Wan, Y.; Samundsett, C.; Bullock, J.; Hettick, M.; Allen, T.; Yan, D.; Peng, J.; Wu, Y.; Cui, J.; Javey, A.; Cuevas, A. Conductive and Stable Magnesium Oxide Electron-Selective Contacts for Efficient Silicon Solar Cells, *Adv. Energy Mater.* **2016**, 1601863, 1-7, https://doi.org/10.1002/aenm.201601863.

[47] Yoshinaga, N.; Kumakura, S.; Kubota, K.; Horiba, T.; Komaba, S. Lithium Magnesium Tungstate Solid as an Additive into $Li(Ni_{1/3}\ Mn_{1/3}\ Co_{1/3})O_2$ Electrodes for Li-Ion Batteries, *J. Electrochem. Soc.* **2019**, 166 (3), A5430-A5436.

[48] Tang, Q.; Zhu, X. Structural Characterization and Physical Properties of Double Perovskite $La_2FeReO_{6+\delta}$ Powders, *Nanomaterials* 2022, 12, 244 4-16. https://doi.org/10.3390/nano12020244.

[49] Nenning, A.; Opitz, A. K.; Rameshan, C.; Rameshan, R.; Blume, R.; Ha¨vecker, M.; Knop-Gericke, A.; Rupprechter, G.; Klo¨tzer, B.; Fleig, J. Ambient Pressure XPS Study of Mixed Conducting Perovskite-Type SOFC Cathode and Anode Materials under Well-Defined Electrochemical Polarization, *J. Phys. Chem.* **2016**, 120, 1462-1471. https://doi.org/acs.jpcc.5b08596.

[50] Crumlin, E. J.; Mutoro, E.; Hong, W. T.; Biegalski, M. D.; Christen, H.M.; Liu, Z.; Bluhm, H.; Shao-Horn, Y. In Situ Ambient Pressure X-ray Photoelectron Spectroscopy of Cobalt Perovskite Surfaces under Cathodic Polarization at High Temperatures. *J. Phys. Chem. C.* **2017**, 2117 (013), 16087−16094.

[51] Sharma, N.; Prabakar, K.; Ilango, S.; Dash, S.; Tyag, A. K. Optical band-gap and associated Urbach energy tails in defected AlN thin films grown by ion beam sputter deposition: Effect of assisted ion energy. *Adv Matter Proc* **2017**, 2(5), 342-346. https://doi.org/10.5185/amp.2017/511.

[52] Amironesei, A.; Airinei, A.; Timpu, D.; Cozan, V.; Rambu, A. P.; Irimia, M.; Iacomi, F.; Rusu, G. I. Electrical and optical properties of some polyazomethine thin films prepared by a spin-coating method, J. Optoelectron. Adv. Mater. **2011**, 13 (7), 802-806.

[53] Prepelita, P.; Medianu, R.; Garoi, F.; Stefan, N.; Iacomi, F. On the structural and electrical characteristics of zinc oxide thin films, *Thin Solid Films* **2010**, 518, 4615–4618. http://dx.doi.org/10.1016/j.tsf.2009.12.044.

[54] John, G. M.; Mugo, S. W.; Ngaruiya, J. M.; Mugambi, N.; Riungu, G. G. Correlation of Bond Energy and Optical Band Energy of Annealed TiO_2 Thin Films, *Am. J. Energy. Res*. **2021**, 9 (1), 1-5. https://doi.org/10.12691/ajer-9-1-1.